Massimo Callegari *
Department of Mechanics,
Polytechnic University of Marche,
Ancona, Italy
m.callegari@univpm.it

Alessandro Cammarata
Department of Industrial and
Mechanical Engineering,
University of Catania, Italy
acamma@diim.unict.it

Andrea Gabrielli
Department of Mechanics,
Polytechnic University of Marche,
Ancona, Italy
andrea.gabrielli@univpm.it

Maurizio Ruggiu
Department of Mechanical
Engineering,
University of Cagliari, Italy
ruggiu@dimeca.unica.it

Rosario Sinatra
Department of Industrial and
Mechanical Engineering,
University of Catania, Italy
rsinatra@diim.unict.it

Analysis and Design of a Spherical Micromechanism with Flexure Hinges

The article describes the design of a robotic wrist able to perform spherical motions: its mechanical architecture is based on parallel kinematics and is suitable to be realized at the mini- or micro-scale by means of flexible joints. In view of the preliminary design, a rigid body model has been studied first and the direct and inverse kinematic analyses have been performed, allowing for the determination of theoretical workspace and passive joints displacements. The rigid body dynamic behavior and the operative ranges of the machine have been assessed through the development of an inverse dynamics model. Then, the micro parts have been designed with the help of FEM and multibody software and the study has been focused on the flexures: since the analyses showed that the centre of the spherical motion moves around several millimeters in the workspace, the original kinematic concept has been modified with the introduction of a ball joint constraining the mobile platform to frame so as to prevent unwanted translations.

1 Introduction

The increasing needs for better accuracy and high performances in manufacturing motivate researchers to develop new classes of parallel manipulators with reduced number of degrees of freedom. These manipulators are designed to accomplish specific tasks where only certain motions are required or must be enabled: in this way more compact and simpler architectures, with respect to six-dof full mobility parallel manipulators, have been devised [1-6]. Of course these machines are not general purpose robots, but they are better addressed to specific applications which they have been built for; however, in these cases, they are composed by a considerably lower number of links and joints and can work with outstanding performances in terms of accuracy, acceleration, thrust or other mechanical characteristics.

The present article describes the design of a mini spherical wrist developed by the Authors within a research project that aimed at exploring the realization of mini devices for the orientation of parts or tools in the space [7]. Of course all the design has been driven by the particular small-scale application. The kinematic synthesis has been steered by the requirement to find a concept mechanism characterized by a spherical motion whose joints were suitable to be realized by the techniques of flexures: of course all usual kinematic performances such as manipulability, dexterity, workspace size, and so on had to be pursued as well.

As a matter of fact, the topic itself of designing parallel kinematics machines, PKM's, able to perform motions of pure rotation, also called Spherical Parallel Machines, SPM's, is quite a recent research subject: besides the most important mechanism of this type, the agile eye by Gosselin and Angeles [8], few other studies on the subject are available during the 90's, e.g. [9-11]. In the new millennium, however, a growing interest on spherical parallel wrists produced many interesting results, as new kinematic architectures or powerful design tools. The use of synthesis methods based on screw theory, for instance, has been exploited by Kong and Gosselin to provide comprehensive listings of both overconstrained and non-overconstrained SPM's [12-13]; Hervé and Karouia, on the other hand, used the theory of Lie group of displacements to generate novel architectures, as the 3-RCC, 3-CCR, 3-CRC kinematics [14] or the four families described in [15]; Fang and Tsai used the theory of reciprocal screws to present a systematic methodology for the structural synthesis of a class of 3-DOF rotational parallel manipulators [16], including the 3-CRU kinematics here analyzed. Other interesting architectures, as the 3-URC, the 3-RUU or the 3-RRS, have been studied by Di Gregorio [17-19] and recently by other researchers; Lusk and Howell, in the end, described a spherical bistable micromechanism [20]. In [21] Callegari analyzed several wrist architectures, then a novel wrist based on the 3-CPU structure has been developed till the prototypal stage; in the present work the 3-CRU variant is considered because, even if it is characterized by a more complex kinematics, it is more suitable to be realized at a mini- or micro- scale.

Many interesting works have been recently published also on the subject of mini or micro-manipulators design, like the fundamental studies [22-24] or the more recent realizations [25-29]. As a matter of fact, the central issue in wrist design has been the proper dimensioning of flexure hinges, whose kineto-elasto-static analysis is of course complicated by the large field of

displacements they undergo [30-31]. In fact the actual stroke of the passive joints, which have a limited deformability, is highly affected by the chosen material and by path planning and can impact seriously the size of the operative workspace. Therefore in the present case joints' design had to be developed together with the dimensioning of manipulator's legs and finally of the whole platform, requiring an integrated kineto-static design.

2 Description of geometry

Figure 1 shows the 3-CRU kinematics of a spherical wrist: the mobile platform is actuated in-parallel by 3 identical legs, each one composed by two links that are joined together by a revolute pair (R); the limbs are connected to the ground by a cylindrical (actuated) joint (C) and to the mobile platform by a universal joint (U). The concept is derived from the spherical 3-CPU mechanism [21] but in this case it has been modified with the substitution of the prismatic pair with a revolute joint in view of a miniature realization by means of flexures.

The wrist is characterized by 3 degrees of freedom, that in the general case yield complex spatial motions: nevertheless, under some geometrical conditions explained in the following section, motions of pure rotation can be achieved. Such conditions are satisfied by the symmetric architecture described in the present article, where the following assumptions have been made: the axes of the 3 base cylindrical joints are orthogonal to each other and intersect at a common point O; the 3 legs are identical and symmetrically disposed; in each leg, the axis of the cylindrical joint is on the same plane of the axis of the second revolute pair of the universal joint, that is directly connected to the mobile platform, whereas the other two revolute joints are normal to this plane; moreover, the axes of the "outer" revolute pairs of the 3 universal joints are orthogonal to each other and intersect in O. The study of the kinematics hereby presented will assume that the actuation of the platform is obtained by directly driving the linear motion in the cylindrical pairs that connect the limbs with the frame: this solution can be effectively realized by separating the constraint posed by the cylindrical pair into its elemental prismatic and revolute components and by driving the slider.

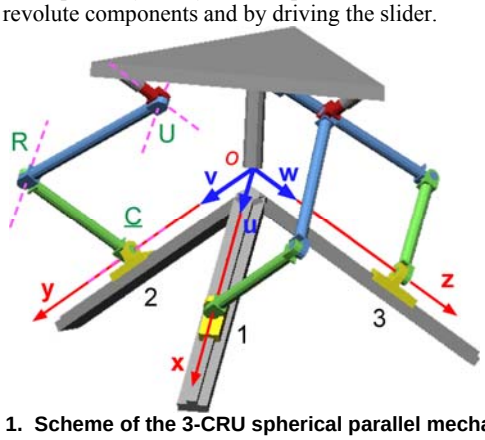

Fig. 1. Scheme of the 3-CRU spherical parallel mechanism

3 Kinematic Analysis

3.1 Congruence equations

Some reference Cartesian frames are now introduced in order to simplify the development of the kinematic relations of the machine, as shown in Fig. 2: the global frame $O(x,y,z)$ is attached to the ground at the point O, with $\{x,y,z\}$ aligned along the cylindrical joints axes; at the same point are also defined 3 further (fixed) local frames $O_i(\boldsymbol{x}_i,\boldsymbol{y}_i,\boldsymbol{z}_i)$, one for each limb, that are rotated with respect to the global frame as defined by the following rotation matrices ${}^{O}_{i}\mathbf{R}$:

$$ {}^{O}_{1}\mathbf{R} = \begin{bmatrix} 1 & 0 & 0 \\ 0 & 1 & 0 \\ 0 & 0 & 1 \end{bmatrix} \quad {}^{O}_{2}\mathbf{R} = \begin{bmatrix} 0 & 0 & 1 \\ 1 & 0 & 0 \\ 0 & 1 & 0 \end{bmatrix} \quad {}^{O}_{3}\mathbf{R} = \begin{bmatrix} 0 & 1 & 0 \\ 0 & 0 & 1 \\ 1 & 0 & 0 \end{bmatrix} \quad (1) $$

The orientation of the mobile platform can be assigned by means of the frame $P(\boldsymbol{u},\boldsymbol{v},\boldsymbol{w})$, whose axes $\boldsymbol{u}$, $\boldsymbol{v}$ and $\boldsymbol{w}$ are aligned with the outer revolute pairs connecting the platform to legs 3, 1 and 2 respectively and intersect at P. A loop closure equation can be set for every limb by moving along its structure and visiting all the joints. The travelling local frame of the ith limb is initially coincident with the fixed local frame: then a translation of a_i along the direction of the $\boldsymbol{x}_i$ axis, allowing for the variable sliding of the cylindrical pair, brings the frame to the point A_i where it is rotated by θ_{1i} around the $\boldsymbol{x}_i$ axis. Then the frame is translated of b along the (current) $\boldsymbol{z}$ axis reaching the point D_i where, for the presence of the revolute joint, it is rotated by θ_{2i} around the (current) $\boldsymbol{y}$ axis. Another translation of c along the (current) $\boldsymbol{z}$ axis brings the travelling frame to the point B_i where the universal joint allows it to rotate by θ_{3i} around the (current) $\boldsymbol{y}$ axis and by θ_{4i} around the (current) $\boldsymbol{z}$ axis respectively. Then the frame is translated of d along the (current) $\boldsymbol{z}$ axis reaching the point P and a further rotation brings it to the location $P(\boldsymbol{u}_i,\boldsymbol{v}_i,\boldsymbol{w}_i)$; after a final rotation by the matrix ${}^{i}_{O}\mathbf{R}$ it is brought to coincide with the frame $P(\boldsymbol{u},\boldsymbol{v},\boldsymbol{w})$, attached to the mobile platform. It will be shown that, with proper mounting conditions, the points P and O can be made to coincide and that in the home pose the frame $P(\boldsymbol{u}_i,\boldsymbol{v}_i,\boldsymbol{w}_i)$ can be aligned with the local fixed frame $O_i(\boldsymbol{x}_i,\boldsymbol{y}_i,\boldsymbol{z}_i)$. Table 1 summarizes the values obtained for the geometrical parameters b, c and d after wrist design and used to draw all the figures.

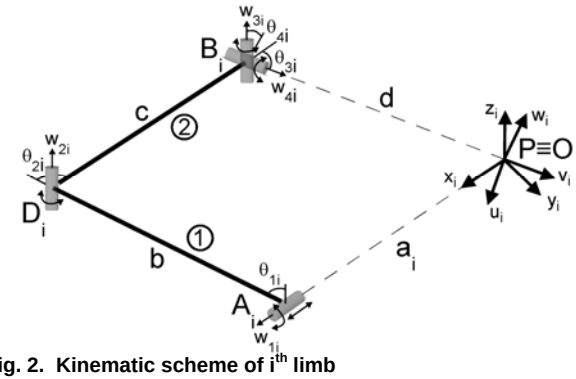

Fig. 2. Kinematic scheme of ith limb

Table 1. Geometrical parameters of the rigid-body 3-CRU wrist

Parameter	Dimension [mm]
b	26.1
c	38.2
d	23.0

3.2 Analysis of mobility

The mobility analysis performed in [32] shows that in order to prevent the 3-CRU mechanism from translating, the following *manufacturing and mounting conditions* must be satisfied:

i. $\hat{\mathbf{w}}_{1i}$ and $\hat{\mathbf{w}}_{4i}$ incident in P

ii. $\hat{\mathbf{w}}_{2i} \perp < \hat{\mathbf{w}}_{1i}, \hat{\mathbf{w}}_{4i} >$ i.e. $\hat{\mathbf{w}}_{2i} \cdot \hat{\mathbf{w}}_{4i} = 0$ and $\hat{\mathbf{w}}_{2i} \cdot \hat{\mathbf{w}}_{1i} = 0$

iii. $\hat{\mathbf{w}}_{3i} \perp < \hat{\mathbf{w}}_{1i}, \hat{\mathbf{w}}_{4i} >$ i.e. $\hat{\mathbf{w}}_{3i} \cdot \hat{\mathbf{w}}_{4i} = 0$ and $\hat{\mathbf{w}}_{3i} \cdot \hat{\mathbf{w}}_{1i} = 0$

In this case the point P does not move in the operative space and the mobile platform just rotates around it without translating. Translation singularities occur when:

$$\hat{\mathbf{w}}_{31} \cdot \hat{\mathbf{w}}_{32} \times \hat{\mathbf{w}}_{33} = 0 \tag{2}$$

i.e. the platform can translate only if the unit vectors $\hat{\mathbf{w}}_{3i}$ of the third revolute joints of each limb i are linearly dependent: this also justifies the choice of mounting the limbs on orthogonal planes when the mobile frame $P(\boldsymbol{u},\boldsymbol{v},\boldsymbol{w})$ is coincident with the fixed one $O(\boldsymbol{x},\boldsymbol{y},\boldsymbol{z})$, since this configuration is the most far away from translation singularities.

3.3 Direct and inverse position kinematics

Position kinematics is solved as usual by writing one loop closure equation for each limb i [32], as shown in Fig. 2:

$$(A_i - P) + (D_i - A_i) + (B_i - D_i) + (P - B_i) = 0 \tag{3}$$

or:

$$\mathbf{a}_i + \mathbf{b}_i + \mathbf{c}_i + \mathbf{d}_i = 0 \tag{4}$$

The **inverse position kinematics** (IPK) is solved by expressing the joint actuation variables a_i, i=1,2,3 as functions of platform orientation (identified by its rotation matrix ${}^{O}_{P}\mathbf{R}$) in the task space. If the wrist is assembled in such a way that, in the home position, each limb is laid as shown in Fig. 1 and the strokes of the joint variables are limited to positive values, the IPK admits only one feasible solution. By calling r_{ij} the element of the rotation matrix, it is obtained:

$$a_i = \sqrt{c^2 - \left(b - d\sqrt{1 - r_{ij}^2}\right)^2} - d \cdot r_{ij} \tag{5}$$

with (i,j) ={(1,2), (2,3), (3,1)}.

Turning to the **direct position kinematics** (DPK), platform orientation in the task space is expressed as a function of joint actuation variables a_i, i=1,2,3:

$$r_{ij} = \frac{-a_i\left(K + a_i^2\right) + \sqrt{-b^2\left(K + a_i^2\right)^2 + 4\left(a_i^2 + b^2\right)b^2 d^2}}{2d\left(a_i^2 + b^2\right)} \tag{6}$$

with (i,j) ={(1,2), (2,3), (3,1)} and $K = d^2 + b^2 - c^2$.

Once the elements r_{12}, r_{23}, r_{31} of the rotation matrix ${}^{O}_{P}\mathbf{R}$ are calculated, the entire rotation matrix can be found: since the problem admits up to 8 solutions, it can be said that for every set of joint actuation variables a_1, a_2, a_3 up to 8 different platform orientations in the task space are allowed.

3.4 Motion range of the passive joints

The assessment of the motion range of passive joints is very important for the present study, since in the final design they have to be realized by means of flexures. The required strokes can be easily worked out [7], once the IPK has been solved in closed-form. Table 2 summarizes the motion range of the passive joints when the wrist is moved throughout its orientation workspace, i.e. the restricted sphere identified in the following section 3.6.

3.5 Differential kinematics and singularities

The velocity of point B_i can be expressed for each limb i in the two following ways:

$$\mathbf{v}_{Bi} = \boldsymbol{\omega} \times (-\mathbf{d}_i) \tag{7}$$

$$\mathbf{v}_{Bi} = \dot{\mathbf{a}}_i + \boldsymbol{\omega}_{1i} \times \mathbf{b}_i + (\boldsymbol{\omega}_{1i} + \boldsymbol{\omega}_{2i}) \times \mathbf{c}_i \tag{8}$$

where $\boldsymbol{\omega}$ is the angular velocity of the mobile platform and $\dot{\mathbf{a}}_i$ is the velocity of the actuation slider. By equating (7) and (8) and collecting the 3 relations for i=1,2,3, the following matrix expression can be obtained:

$${}^{O}\mathbf{J}_D \cdot {}^{O}\boldsymbol{\omega} = {}^{O}\mathbf{J}_I \cdot \dot{\mathbf{a}} \tag{9}$$

The mapping between the angular velocity of the platform expressed in the global frame ${}^{O}\boldsymbol{\omega} = [\omega_x \quad \omega_y \quad \omega_z]^T$ and the rates of actuated variables $\dot{\mathbf{a}} = [\dot{a}_1 \quad \dot{a}_2 \quad \dot{a}_3]^T$ is provided by means of the *direct Jacobian matrix* ${}^{O}\mathbf{J}_D$ and *inverse Jacobian matrix* ${}^{O}\mathbf{J}_I$:

$${}^{O}\mathbf{J}_D = d\begin{bmatrix} \left({}^{O}\hat{\mathbf{c}}_1 \times {}^{O}\hat{\mathbf{d}}_1\right)^T \\ \left({}^{O}\hat{\mathbf{c}}_2 \times {}^{O}\hat{\mathbf{d}}_2\right)^T \\ \left({}^{O}\hat{\mathbf{c}}_3 \times {}^{O}\hat{\mathbf{d}}_3\right)^T \end{bmatrix} \qquad {}^{O}\mathbf{J}_I = \begin{bmatrix} \hat{\mathbf{c}}_1^T \cdot \hat{\mathbf{a}}_1 & 0 & 0 \\ 0 & \hat{\mathbf{c}}_2^T \cdot \hat{\mathbf{a}}_2 & 0 \\ 0 & 0 & \hat{\mathbf{c}}_3^T \cdot \hat{\mathbf{a}}_3 \end{bmatrix} \tag{10}$$

The vectors in (10) can be evaluated in the base frame in order to compute the elements of ${}^{O}\mathbf{J}_D$ and ${}^{O}\mathbf{J}_I$:

$${}^{O}\mathbf{J}_D = d\begin{bmatrix} 0 & c\theta_{11}s\theta_{31} & s\theta_{11}s\theta_{31} \\ s\theta_{12}s\theta_{32} & 0 & c\theta_{12}s\theta_{32} \\ c\theta_{13}s\theta_{33} & s\theta_{13}s\theta_{33} & 0 \end{bmatrix} \quad {}^{O}\mathbf{J}_I = \begin{bmatrix} s\theta_{21} & 0 & 0 \\ 0 & s\theta_{22} & 0 \\ 0 & 0 & s\theta_{23} \end{bmatrix} \tag{11-12}$$

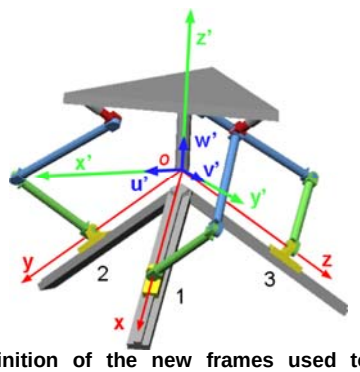

Fig. 3. Definition of the new frames used to define the operative workspace of the wrist

Table 2. Motion range of the passive joints (rigid body model)

	$\boldsymbol{\theta}_{1i}$			$\boldsymbol{\theta}_{2i}$			$\boldsymbol{\theta}_{3i}$			$\boldsymbol{\theta}_{4i}$		
	$\boldsymbol{\theta}_{1i}^{(\min)}$	$\boldsymbol{\theta}_{1i}^{(\max)}$	$\Delta\boldsymbol{\theta}_{1i}$	$\boldsymbol{\theta}_{2i}^{(\min)}$	$\boldsymbol{\theta}_{2i}^{(\max)}$	$\Delta\boldsymbol{\theta}_{2i}$	$\boldsymbol{\theta}_{3i}^{(\min)}$	$\boldsymbol{\theta}_{3i}^{(\max)}$	$\Delta\boldsymbol{\theta}_{3i}$	$\boldsymbol{\theta}_{4i}^{(\min)}$	$\boldsymbol{\theta}_{4i}^{(\max)}$	$\Delta\boldsymbol{\theta}_{4i}$
i = 1	-32.0°	+29.2°	61.2°	-5.1°	0°	5.1°	-26.4°	+36.7°	63.1°	-29.2°	+32.0°	61.2°
i = 2	-29.2°	+32.0°	61.2°	-5.3°	0°	5.3°	-26.7°	+33.6°	60.3°	-31.6°	+31.5°	63.1°
i = 3	-31.6°	+31.5°	63.1°	-5.3°	0°	5.3°	-24.8°	+37.3°	62.1°	-32.0°	+29.2°	61.2°

In order to improve the clearness of the following steps, leading to the definition of wrist workspace, two new reference frames are introduced, as defined in Fig. 3; the fixed frame $O'(\boldsymbol{x'},\boldsymbol{y'},\boldsymbol{z'})$ is obtained by means of the following rotation of the old frame $O(\boldsymbol{x},\boldsymbol{y},\boldsymbol{z})$:

$$ {}^{O}_{O'}\mathbf{R} = \frac{\sqrt{6}}{6}\begin{bmatrix} 1 & \sqrt{3} & -\sqrt{2} \\ 1 & -\sqrt{3} & -\sqrt{2} \\ -2 & 0 & -\sqrt{2} \end{bmatrix} \tag{13} $$

The pose of the mobile platform in the space is now provided by assigning the rotation matrix ${}^{O'}_{P'}\mathbf{R}$ between the mobile frame $P'(\boldsymbol{u'},\boldsymbol{v'},\boldsymbol{w'})$ and the global fixed frame $O'(\boldsymbol{x'},\boldsymbol{y'},\boldsymbol{z'})$; if this matrix is expressed by the Tait-Bryan angles (rotations around the body axes $\boldsymbol{x}$, $\boldsymbol{y}$ and then $\boldsymbol{z}$ of the angles φ, θ, ψ respectively) it holds:

$$ {}^{O'}_{P'}\mathbf{R} = \begin{bmatrix} c\theta c\psi & -c\theta s\psi & s\theta \\ s\varphi s\theta c\psi + c\varphi s\psi & -s\varphi s\theta s\psi + c\varphi c\psi & -s\varphi c\theta \\ -c\varphi s\theta c\psi + s\varphi s\psi & c\varphi s\theta s\psi + s\varphi c\psi & c\varphi c\theta \end{bmatrix} \tag{14} $$

The relation between ${}^{O}_{P}\mathbf{R}$ and the new rotation matrix ${}^{O'}_{P'}\mathbf{R}$ is the following:

$$ {}^{O}_{P}\mathbf{R} = {}^{O}_{O'}\mathbf{R} \cdot {}^{O'}_{P'}\mathbf{R} \cdot {}^{P'}_{P}\mathbf{R} \tag{15} $$

As said in the analysis of mobility, conditions (i-iii) in section 3.2 are not verified, i.e. the wrist occurs in translation singularities, if and only if the three unit vectors $\mathbf{w}_{3i}$ are linearly dependent. By projecting the vectors in (2) in the global frame $O(\boldsymbol{x},\boldsymbol{y},\boldsymbol{z})$ it is obtained:

$$ {}^{O}\mathbf{w}_{31} \cdot {}^{O}\mathbf{w}_{32} \times {}^{O}\mathbf{w}_{33} = c\theta_{11}c\theta_{12}c\theta_{13} + s\theta_{11}s\theta_{12}s\theta_{13} = 0 \tag{16} $$

After few manipulations, the singular configurations in (16) yields:

$$ r_{11}r_{22}r_{33} - r_{32}r_{13}r_{21} = 0 \tag{17} $$

An alternative expression of the *translation singularity surface* (17) can be obtained in the new $O'(\boldsymbol{x'},\boldsymbol{y'},\boldsymbol{z'})$ frame, in function of the introduced Tait-Bryan angles, by using (13-15):

$$ \begin{aligned} &\left[c\theta c\psi + \sqrt{3}\left(s\varphi s\theta c\psi + c\varphi s\psi\right) - \sqrt{2}\left(-c\varphi s\theta c\psi + s\varphi s\psi\right)\right]\cdot \\ &\cdot\left[-c\theta s\psi + \sqrt{3}\left(s\varphi s\theta s\psi - c\varphi c\psi\right) - \sqrt{2}\left(c\varphi s\theta s\psi + s\varphi c\psi\right)\right]\cdot \\ &\cdot\left[2s\theta + \sqrt{2}c\varphi c\theta\right] + \\ &+\left[2c\theta s\psi - \sqrt{2}\left(c\varphi s\theta s\psi + s\varphi c\psi\right)\right]\cdot\left[s\theta - \sqrt{3}s\varphi c\theta - \sqrt{2}c\varphi c\theta\right]\cdot \\ &\cdot\left[c\theta c\psi - \sqrt{3}\left(s\varphi s\theta c\psi + c\varphi s\psi\right) + \sqrt{2}\left(c\varphi s\theta c\psi - s\varphi s\psi\right)\right] = 0 \end{aligned} \tag{18} $$

It is interesting to note from (18) that if the manufacturing and mounting conditions in 3.2 are satisfied, the singularity surface does not depend on the geometrical parameters of the wrist, i.e. the singularities cannot be avoided or moved out of the working space by design. Figure 4 maps the left hand side of (18) for given values of ψ (*0°, 40°* and *90°*): the regions where such expression approaches zero are painted black.

In order to identify the direct and inverse kinematics singularities of the wrist, the velocity mapping (9) is reformulated as:

$$ d^2\begin{bmatrix} 0 & -r_{32}\cdot s\theta_{31} & r_{22}\cdot s\theta_{31} \\ r_{33}\cdot s\theta_{32} & 0 & -r_{13}\cdot s\theta_{32} \\ -r_{21}\cdot s\theta_{33} & r_{11}\cdot s\theta_{33} & 0 \end{bmatrix}\begin{bmatrix} \omega_x \\ \omega_y \\ \omega_z \end{bmatrix} = \begin{bmatrix} s\theta_{21}\left(b + c\cdot c\theta_{21}\right) & 0 & 0 \\ 0 & s\theta_{22}\left(b + c\cdot c\theta_{22}\right) & 0 \\ 0 & 0 & s\theta_{23}\left(b + c\cdot c\theta_{23}\right) \end{bmatrix}\begin{bmatrix} \dot{a}_1 \\ \dot{a}_2 \\ \dot{a}_3 \end{bmatrix} \tag{19} $$

Inverse kinematics singularities are found by letting the following determinant vanish:

$$ s\theta_{21}s\theta_{22}s\theta_{23}\left(b + c\cdot c\theta_{21}\right)\left(b + c\cdot c\theta_{22}\right)\left(b + c\cdot c\theta_{23}\right) = 0 \tag{20} $$

Direct kinematics singularities appear when:

$$ s\theta_{31}s\theta_{32}s\theta_{33}\left(r_{11}r_{22}r_{33} - r_{32}r_{13}r_{21}\right) = 0 \tag{21} $$

that shows that they are a superset of translation singularities.

3.6 Identification of the workspace

The identification of the useful workspace of the robot is very important for its performances and can be optimized by a proper design. Inside this region, taking into account the limited strokes of the actuated joints, the path of the wrist can be freely planned without passing through singularity surfaces. It must be noted that the device can achieve up to 8 different configurations in the operative space (φ,θ,ψ) corresponding to the same set of joints displacements.

By simple geometrical considerations it is seen that when the actuators reach the maximum stroke equal to $a_{\max} = \sqrt{(c+d)^2 - b^2}$ the wrist gets stuck in a singular configuration characterized by the parallelism of the vectors **c** and **d**. Therefore by limiting the travel of the actuated prismatic pairs within the reasonable range:

$$ 0 \le a \le 0.9 \cdot a_{\max} \tag{22} $$

it is possible to identify the corresponding volume in the Tait-Bryan angles space. All the mentioned limit surfaces, i.e. (18) and (20-22), have quite complex shapes, that can be hardly visualized in the operative space (φ,θ,ψ) and sometimes one intersects the others. In order to appreciate qualitatively the constraints posed to workspace boundaries by the singularities surfaces and the limited stroke of the actuators, the maximum sphere inscribed inside each one of them can be computed. By comparing the radiuses of all the spheres, see Fig. 5a, it turns out that, with the chosen geometrical parameters of Tab. 1, the safe workspace of the wrist for motion planning lies inside a sphere of *31°* radius, that is obtained by limiting the stroke of the actuators.

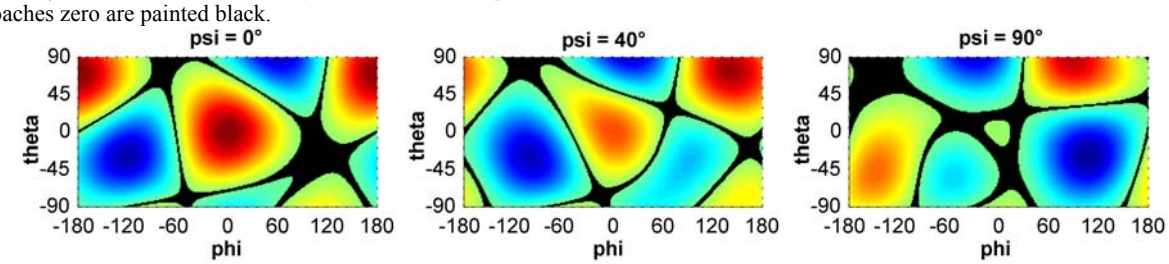

Fig. 4. Translation singularities maps for ψ equal to 0°, 40° and 90°

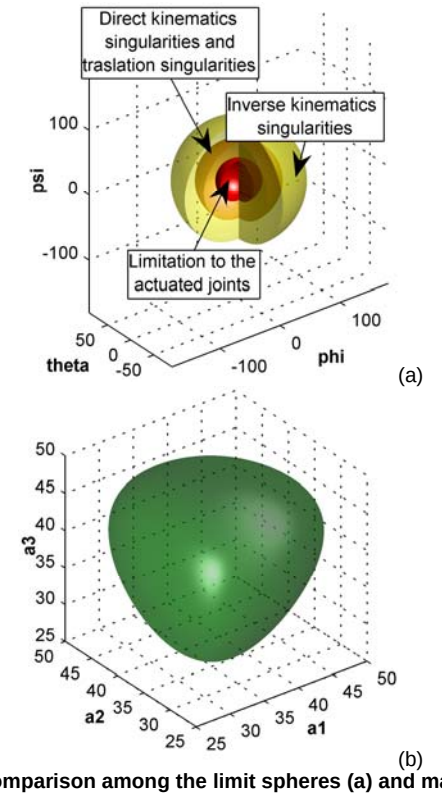

Fig. 5. Comparison among the limit spheres (a) and mapping of the inner sphere into the joint space (b)

Of course, in order to plan properly the motion of the device, such inner sphere of wrist workspace should be better mapped in the space of joint actuation variables a_i, i=1,2,3: by applying the inverse orientation kinematics to the boundary points, the connected and convex surface shown in Fig. 5b is obtained. It is interesting to note that such surface has a quite simple shape also in the joint space. Finally, it is observed that the scheme that has been used for representation and quantification of workspace volume is rather conservative and higher volumes would certainly be disclosed by more refined representations: on the other hand, a pretty simple criterion was needed for preliminary wrist design and related optimization, while the following structural analysis showed that more severe limitations to wrist mobility arise for the use of flexure technique itself.

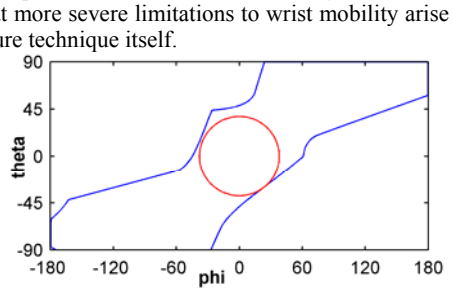

Fig. 6. Subspace generated by the limited stroke of the actuators for ψ = 0

For instance, in case the robot is used as a pointing device, the third rotation ψ around the ***w'*** axis can be null: in this case the useful workspace in the (φ,θ) plane is larger (see Fig. 6, with workspace boundary drawn in blue): it is noted that a circle with a radius approximately equal to *38°* can be inscribed in it. If the third rotation ψ is not important for the application, e.g. handling of a camera, the redundancy of the kinematics could be exploited to overcome singularities and increase dexterity through optimization of the path planning.

4 Static Analysis

By evaluating the *total Jacobian matrix* ${}^{O'}\mathbf{J}={}^{O}\mathbf{J}_I^{-1}\cdot{}^{O}\mathbf{J}_D\cdot{}^{O}_{O'}\mathbf{R}$ in frame *O'*, the force vector $\boldsymbol{\tau}$ of the actuated joints that balances the moment **M** applied at the mobile platform is easily obtained:

$$\dot{\mathbf{a}}={}^{O'}\mathbf{J}\cdot{}^{O'}\boldsymbol{\omega} \tag{23}$$

$$\boldsymbol{\tau}={}^{O'}\mathbf{J}^{-T}\cdot{}^{O'}\mathbf{M} \tag{24}$$

A typical way of visualizing the static performances of a manipulator is to draw the *ellipsoids of manipulability*, obtained by constraining the vector of the forces $\boldsymbol{\tau}$ in a unitary radius sphere:

$$\boldsymbol{\tau}^T\cdot\boldsymbol{\tau}=1 \tag{25}$$

The equation of the ellipsoid in the (φ,θ,ψ) space is obtained by substituting (24) in (25):

$${}^{O'}\mathbf{M}^T\cdot\left({}^{O'}\mathbf{J}^{T\,O'}\mathbf{J}\right)^{-1}\cdot{}^{O'}\mathbf{M}=1 \tag{26}$$

The ellipsoid matrix $\left({}^{O'}\mathbf{J}^{T\,O'}\mathbf{J}\right)^{-1}$ is symmetric and positive semi-definite, therefore its eigenvectors are orthogonal and coincide with the principal axes of the ellipsoid; moreover, the half-lengths of the principal axes m_i are equal to the square roots of the eigenvalues λ_i of ${}^{O'}\mathbf{J}^{T\,O'}\mathbf{J}$:

$$m_i=\frac{1}{\sqrt{\lambda_i\left[\left({}^{O'}\mathbf{J}^{T}\cdot{}^{O'}\mathbf{J}\right)^{-1}\right]}}=\sqrt{\lambda_i\left({}^{O'}\mathbf{J}^{T}\cdot{}^{O'}\mathbf{J}\right)}\qquad \text{for } i=1,2,3 \tag{27}$$

In isotropic configurations the ellipsoid becomes a sphere and the wrist has the highest manipulability, while it degenerates into a planar ellipse in singular configurations. Figure 7 plots the manipulability ellipsoids of the rigid-body wrist under design: it is evident that the symmetrical structure of the manipulator causes a symmetry in the static performances of the machine. The isotropic point is coincident with the home configuration, while the thinning of the ellipsoids outer poses shows that the wrist is approaching workspace boundaries.

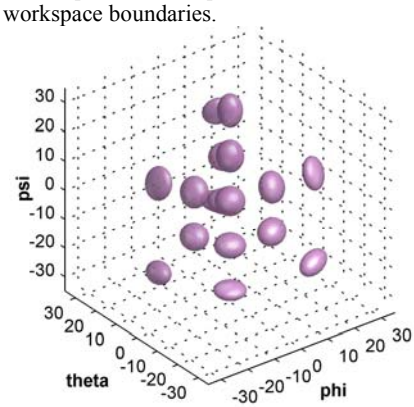

Fig. 7. Ellipsoids of manipulability of force in the Tait-Bryan angles space

Another way of visualizing the dexterity of the wrist is using the condition number k_F, which is the weighted Frobenius norm [33] of the matrix ${}^{O'}\mathbf{J}^{T\,O'}\mathbf{J}$:

$$k_F({}^{O'}\mathbf{J})=\frac{1}{3}\sqrt{tr\left({}^{O'}\mathbf{J}^{T\,O'}\mathbf{J}\right)\cdot tr\left[\left({}^{O'}\mathbf{J}^{T\,O'}\mathbf{J}\right)^{-1}\right]} \tag{28}$$

It is noted that the condition number of wrist's Jacobian k_F, like any form of condition number, is bounded from below but

unbounded from above, i.e. $1 \le k_F\left({}^{O'}\mathbf{J}\right) < \infty$: of course in correspondence of an isotropic point it equals 1, while it approaches ∞ when the robot gets close to a point of singularity.

Figure 8 maps the dexterity of the wrist under design: in order to obtain a good graphic rendering, the value of $k_F^{-1}\left({}^{O'}\mathbf{J}\right)$ is plotted for given values of ψ : the regions where such expression approaches zero are painted black and identify the singularities.

It can be seen that few isotropic attitudes can be identified within the workspace, but there is at maximum one such isolated point for each singularity free region: moreover, due to symmetry reasons, the region including the (isotropic) home configuration is the one having the maximum average dexterity within the largest volume and therefore the most suitable to be selected for planning the tasks of the wrist. It is also interesting to note that inside the chosen inner workspace (i.e. a sphere of radius equal to *31°* in the φ,θ,ψ space) the value of $k_F^{-1}\left({}^{O'}\mathbf{J}\right)$ is always greater than 0.8, see Fig. 9, so that the robot is constantly close to the condition of isotropy.

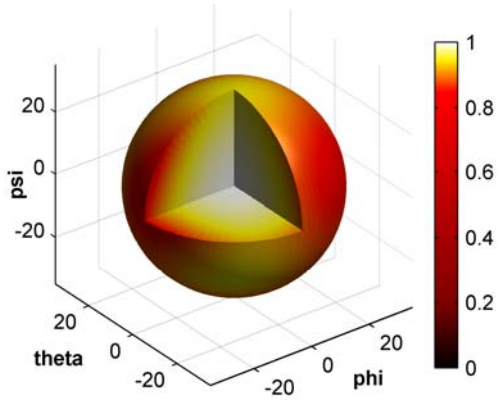

Fig. 9. Mapping of the inverse of the condition number, $k_F^{-1}\left({}^{O'}\mathbf{J}\right)$, inside the restricted workspace

5 Robot Dynamics

Robot dynamics has been analyzed by means of the Natural Orthogonal Complement (NOC) approach, that allowed to obtain the dynamic equations in the Euler-Lagrange form without the need to remove explicitly the constraint forces and torques among bodies [34-35]. This operation has been carried out by using the *twist shaping matrix* **T**, that is orthogonal to the constraints matrix of a holonomic mechanical system.

Firstly, the twists of the seven bodies composing the (rigid body) 3-CRU wrist have been worked out, then the rates of the passive joint-angles have been derived. Finally, the twist shaping matrices of each link and of the moving platform have been calculated and assembled into the final model. Details of the procedure are explained in reference [32].

5.1 Dynamics model

The equations of wrist's dynamics are expressed in the joint space as:

$$\boldsymbol{\tau}_a + \boldsymbol{\tau}_g = \mathbf{I}\ddot{\mathbf{a}} + \mathbf{C}\dot{\mathbf{a}} \tag{29}$$

where **I** is the generalized inertia matrix, **C** is the Coriolis and centrifugal forces vector, $\boldsymbol{\tau}_a$ is the vector of actuation forces and $\boldsymbol{\tau}_g$ are the generalized gravitational forces acting on the actuators. It is noted that friction and damping forces have been neglected.

In order to compute **I**, the mass dyad $\mathbf{M}_i$ of each link is considered:

$$\mathbf{M}_i = \begin{bmatrix} \mathbf{J}_i & \mathbf{O}_3 \\ \mathbf{O}_3 & m_i\mathbf{I}_3 \end{bmatrix} \tag{30}$$

where m_i and $\mathbf{J}_i$ are respectively the mass and inertia matrix of *i-th* body. Through the twist shaping matrices $\mathbf{T}_i$ the generalized inertia matrix is composed in the following way:

$$\mathbf{I} = \sum_{i=1}^{3}\left(\mathbf{T}_{1i}^T \cdot \mathbf{M}_{1i} \cdot \mathbf{T}_{1i} + \mathbf{T}_{2i}^T \cdot \mathbf{M}_{2i} \cdot \mathbf{T}_{2i}\right) + \mathbf{T}_P^T \cdot \mathbf{M}_P \cdot \mathbf{T}_P \tag{31}$$

where each matrix has been expressed into the global reference system.

In order to obtain the Coriolis and centrifugal forces vector **C,** the time-rates $\dot{\mathbf{T}}_i$ of the twist shaping matrices $\mathbf{T}_i$ must be computed. Unfortunately the related symbolic expressions are very complex, therefore a numeric derivation has been used in order to optimize and reduce computational time. In matrix form the vector **C** is evaluated as:

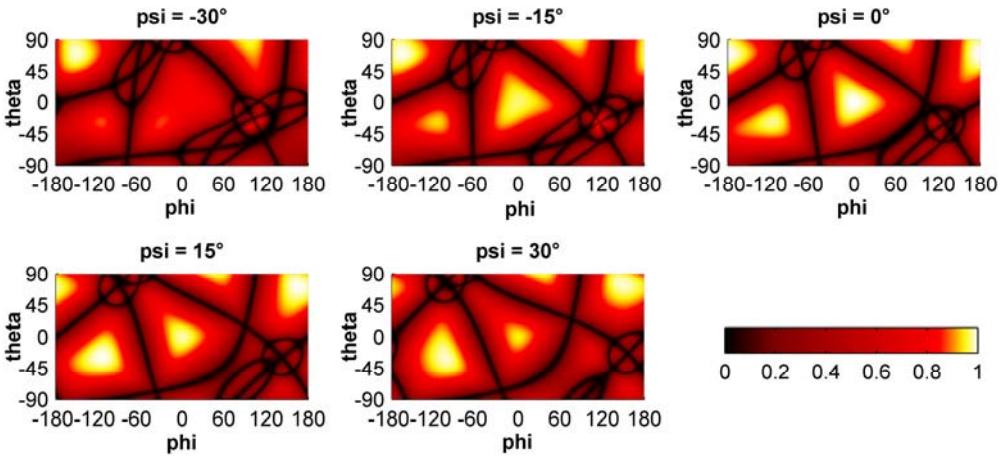

Fig. 8. Mapping of the inverse of the condition number, $k_F^{-1}\left({}^{O'}\mathbf{J}\right)$, for ψ equal to -30°, -15°, 0°, 15° and 30°

Table 3. Mass parameters of the (rigid-body) 3-CRU wrist

link	mass [kg]	center of mass position [mm]	inertia matrix [kg mm^2]
Lower limb (1)	$m_1 = 0.0043$	$\mathbf{c}_{g1i} = [0 \quad 0 \quad 13.1]^T$	$\mathbf{J}_1 = \begin{bmatrix} 0.157 & 0 & 0.029 \\ 0 & 0.160 & 0 \\ 0.029 & 0 & 0.030 \end{bmatrix}$
Upper limb (2)	$m_2 = 0.0063$	$\mathbf{c}_{g2i} = [0 \quad 0 \quad 19.1]^T$	$\mathbf{J}_2 = \begin{bmatrix} 0.336 & 0 & -0.089 \\ 0 & 0.343 & 0 \\ -0.089 & 0 & 0.075 \end{bmatrix}$
Platform	$m_P = 0.1048$	$\mathbf{c}_{gP} = -\begin{bmatrix} \sqrt{3}/3 & \sqrt{3}/3 & \sqrt{3}/3 \end{bmatrix}^T \cdot 18.9$	$\mathbf{J}_P = \begin{bmatrix} 57.276 & -13.508 & -13.508 \\ -13.508 & 57.276 & -13.508 \\ -13.508 & -13.508 & 57.276 \end{bmatrix}$

$$\mathbf{C} = \sum_{i=1}^{3} \left(\mathbf{T}_{1i}^T \cdot \mathbf{W}_{1i} \cdot \mathbf{M}_{1i} \cdot \mathbf{T}_{1i} + \mathbf{T}_{2i}^T \cdot \mathbf{W}_{2i} \cdot \mathbf{M}_{2i} \cdot \mathbf{T}_{2i} + \right.$$
$$\left. + \mathbf{T}_{1i}^T \cdot \mathbf{M}_{1i} \cdot \dot{\mathbf{T}}_{1i} + \mathbf{T}_{2i}^T \cdot \mathbf{M}_{2i} \cdot \dot{\mathbf{T}}_{2i} \right) + \mathbf{T}_P^T \cdot \mathbf{W}_P \cdot \mathbf{M}_P \cdot \mathbf{T}_P + \mathbf{T}_P^T \cdot \mathbf{M}_P \cdot \dot{\mathbf{T}}_P \tag{32}$$

where $\mathbf{W}_{ji}$ (j = 1,2; i = 1,2,3) are the angular velocities dyads:

$$\mathbf{W}_{ji} = \begin{bmatrix} \mathbf{\Omega}_{ji} & \mathbf{O}_3 \\ \mathbf{O}_3 & \mathbf{O}_3 \end{bmatrix} \tag{33}$$

and $\mathbf{\Omega}_{ji}$ is the cross product matrix of the angular velocities vector $\boldsymbol{\omega}_{ji}$ of each body.

The generalized gravitational and active forces are now computed; to this aim, all the wrenches acting on the mass centre of each body must be evaluated. The gravitational wrenches of the mobile platform and of the *k-th* link of the *i-th* limb are respectively:

$$\mathbf{w}_{G_P} = \begin{bmatrix} \mathbf{0}_{3\times1} \\ m_P \mathbf{g} \end{bmatrix} \qquad \mathbf{w}_{G_{ki}} = \begin{bmatrix} \mathbf{0}_{3\times1} \\ m_{ki} \mathbf{g} \end{bmatrix} \quad k = 1,2 \quad i = 1,2,3 \tag{34-35}$$

Then, in order to obtain the correspondent generalized forces $\boldsymbol{\tau}_{g_P}$ and $\boldsymbol{\tau}_{g_{ki}}$, the generic wrenches $\mathbf{w}_{G_P}$ $\mathbf{w}_{G_{ki}}$ must be multiplied by the corresponding transposed twist shaping matrices $\mathbf{T}_P$ and $\mathbf{T}_{ki}$, i.e.:

$$\boldsymbol{\tau}_{g_P} = \mathbf{T}_P^T \mathbf{w}_{G_P} \quad \text{and} \quad \boldsymbol{\tau}_{g_{ki}} = \mathbf{T}_{ki}^T \mathbf{w}_{G_{ki}} \tag{36}$$

Finally, all the components are summed up in order to obtain the global generalized gravitational force $\boldsymbol{\tau}_g$. In the same way the global generalized active force $\boldsymbol{\tau}_a$ can be computed.

5.2 Inverse dynamics equations

The inverse dynamics model of the 3-CRU wrist has been studied in simulation in order to verify the model and to assess the effects of machine's dynamics on global performances. A first set of simulations has been aimed at evaluating the relative contribution of the terms that are summed up in robot dynamics model; once the task space trajectory had been fixed, the analysis has been focused on the effects of inertia, centrifugal and Coriolis' forces, by plotting the following terms:

1. $\boldsymbol{\tau}_a = \mathbf{I}\ddot{\mathbf{a}} + \mathbf{C}\dot{\mathbf{a}} - \boldsymbol{\tau}_g$ complete expression of wrist dynamics
2. $\boldsymbol{\tau}_{aC} = \mathbf{I}\ddot{\mathbf{a}} - \boldsymbol{\tau}_g$ absence of Coriolis' wrench
3. $\boldsymbol{\tau}_{aS} = -\boldsymbol{\tau}_g$ static forces only

Table 3 collects the mass parameters that have been used for the simulations: they correspond to the final design of the flexible-body model of the 3-CRU wrist, that will be explained in following section; the geometrical parameters had been presented already in Tab. 1, while the positions of the centers of mass and the inertia tensors of the limbs are expressed in local frames centered in A_i and D_i respectively with longitudinal z axis and transversal x axis; moreover, the position of the center of mass and the inertia matrix of the platform are expressed in the local frame $P(\boldsymbol{u,v,w})$. The following sample trajectories have been imposed in the Tait-Bryan angles space for orienting the mobile platform:

$$\begin{aligned} \varphi &= -\frac{\pi}{10} \cdot \cos(2\pi f \cdot time) \\ \theta &= \frac{\pi}{7} \cdot \sin(2\pi f \cdot time) \\ \psi &= -\frac{\pi}{12} \cdot \cos(2\pi f \cdot time) \end{aligned} \tag{37}$$

where the frequency f has been set equal to *0.1, 1* and *10 Hz* in three different simulation runs. Figure 10 shows that the differences among the three forces $\boldsymbol{\tau}_a$, $\boldsymbol{\tau}_{aS}$, $\boldsymbol{\tau}_{aC}$ here computed are significant only for high speed motions. For instance, when the frequency of the movements is low, e.g. lower than *0.1 Hz*, see Fig. 10a, the contribution of dynamic terms is negligible: this behavior is due to the lightweight structure of the wrist and as a matter of fact suggests to rely on the static analysis only for the evaluation of the forces and the selection of actuators. The Coriolis and centrifugal effects become relevant only for high speed movements: Fig. 10b shows that when their frequency approaches the value of *1 Hz* the three terms $\boldsymbol{\tau}_a$, $\boldsymbol{\tau}_{aS}$, $\boldsymbol{\tau}_{aC}$ can be clearly distinguished. If speeds and accelerations are increased even more, see Fig. 10c drawn for *f=10 Hz*, the gravitational effects can be neglected and machine dynamics becomes overwhelming.

Moreover, in view of wrist design, a thrust of *0.5 N* seems suitable to drive the machine when the prescribed motion is attained with frequencies lower than *1 Hz*: it will be shown at the end of next section that much greater forces are needed anyhow to overcome the elastic reactions in case flexure hinges are used. In case greater speeds should be attained by the wrist, a reliable dynamic model could not do without considering the elastic behavior of links and flexures and therefore should incorporate the capability to perform a vibration analysis.

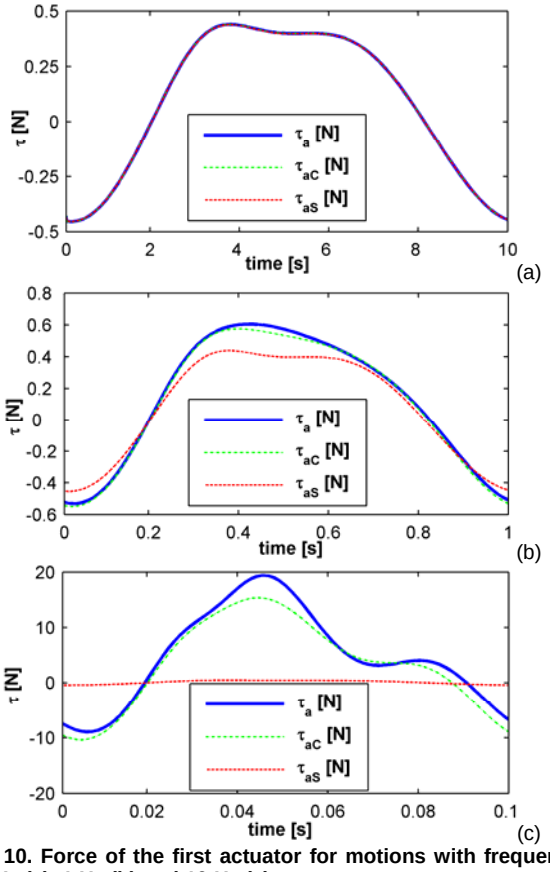

Fig. 10. Force of the first actuator for motions with frequency 0.1 Hz (a), 1 Hz (b) and 10 Hz (c)

The dynamic manipulability ellipsoids introduced by Yoshikawa [38-39] are a useful means to study the dynamic properties of a mechanism: they express graphically the capability of the wrist to yield angular accelerations in all the directions stemming from one attitude of its workspace. As a matter of fact, many other measures of manipulability have been proposed by different researchers since that pioneering work but very few applications dealt with orienting devices.

Let us consider all the actuation forces $\boldsymbol{\tau}_a$ with unit norm:

$$\boldsymbol{\tau}_a^T \cdot \boldsymbol{\tau}_a = 1 \tag{38}$$

By differentiating the velocity mapping (23) it is obtained:

$$\ddot{\mathbf{a}} = \dot{\mathbf{J}} \cdot \boldsymbol{\omega} + \mathbf{J} \cdot \dot{\boldsymbol{\omega}} \tag{39}$$

Now by substituting (39) into (29) it is possible to relate the forces in the joint space to the angular accelerations in the operative space:

$$\boldsymbol{\tau}_a = \mathbf{I}\dot{\mathbf{J}} \cdot \boldsymbol{\omega} + \mathbf{I}\mathbf{J} \cdot \dot{\boldsymbol{\omega}} + \mathbf{C}\dot{\mathbf{a}} - \boldsymbol{\tau}_g = \mathbf{I}\mathbf{J} \cdot \left(\dot{\boldsymbol{\omega}} + \dot{\boldsymbol{\omega}}_{bias}\right) \tag{40}$$

having defined:

$$\dot{\boldsymbol{\omega}}_{bias} = \mathbf{J}^{-1}\dot{\mathbf{J}} \cdot \boldsymbol{\omega} + \mathbf{J}^{-1}\mathbf{I}^{-1}\left(\mathbf{C}\dot{\mathbf{a}} - \boldsymbol{\tau}_g\right) \tag{41}$$

The constraint expressed by (38) can now be written in the following quadratic form:

$$\dot{\boldsymbol{\Omega}}^T \cdot \boldsymbol{\Gamma}(\boldsymbol{\varphi}) \cdot \dot{\boldsymbol{\Omega}} = 1 \tag{42}$$

with obvious meaning of the newly introduced terms:

$$\dot{\boldsymbol{\Omega}} = \dot{\boldsymbol{\omega}} + \dot{\boldsymbol{\omega}}_{\text{bias}} = \dot{\boldsymbol{\omega}} + \mathbf{J}^{-1}\dot{\mathbf{J}} \cdot \boldsymbol{\omega} + \mathbf{J}^{-1}\mathbf{I}^{-1}\left(\mathbf{C}\dot{\mathbf{a}} - \boldsymbol{\tau}_g\right) \tag{43}$$

$$\boldsymbol{\Gamma}(\boldsymbol{\varphi}) = \mathbf{J}^T \cdot \mathbf{I}^T \cdot \mathbf{I} \cdot \mathbf{J} \tag{44}$$

The quadratic form (42) represents the *dynamic manipulability ellipsoid* in the Cartesian space of the angular accelerations: the inspection of (42-44) shows that the presence of gravity and velocity merely induce a translation of the ellipsoid centre in the accelerations space, even if their effects are difficult to evaluate. Making reference to the remarkable case of a fixed platform ($\boldsymbol{\omega}=\mathbf{0}$) in absence of gravity actions ($\boldsymbol{\tau}_g=\mathbf{0}$), (42) provides:

$$\dot{\boldsymbol{\omega}}^T \cdot \boldsymbol{\Gamma}(\boldsymbol{\varphi}) \cdot \dot{\boldsymbol{\omega}} = 1 \tag{45}$$

The quadratic form $\boldsymbol{\Gamma}$ determines the volume and the principal axes of the ellipsoid: in fact, the three principal axes, which represent the maximum and minimum accelerations that can be developed with unit actuator forces, are given by the reciprocal of the square root of the eigenvalues of $\boldsymbol{\Gamma}$ while the eigenvectors represent the associated directions in the orientation space. Figure 11 plots some dynamic manipulability ellipsoids of the robot in the Tait-Bryan angle space; it is noted that twisting accelerations around the *z'* axis are obtained more easily than all other rotations throughout the operative space: such anisotropy is partly due to the active moment generated around the platform by actuators' thrusts (and therefore highly depends on machine kinematics) and partly to the distribution of the masses of limbs and platform: the anisotropy coming from latter contribution could be mitigated by a proper mounting of the part or end-effector on the platform itself.

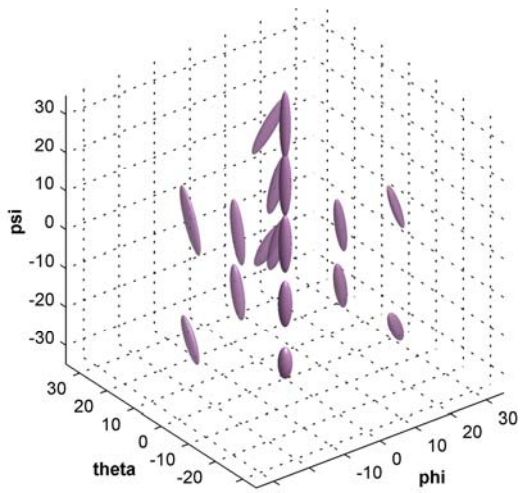

Fig. 11. Dynamic ellipsoids of manipulability of the wrist in the Tait-Bryan angles space

6 Design of the robot

It has been already shown that, when the 3-CRU wrist is made by rigid links, it is characterized by 3 degrees of freedom: however, when compliant joints are used, a rigid-body analysis of the monolithic manipulator shows it to be nine times over-constrained, which explains the difficulties in granting the desired spherical motion: in fact, a kineto-elasto-static analysis of the flexure-based SPM [7] shows that the displacement of the centre *C* of the (theoretical) spherical motion is quite large, in worst cases reaching as much as 80% of the displacement imposed to the actuated pairs. Therefore, in order to guarantee the spherical rotation of the moving platform around *C*, its linear displacements have been constrained by using an extra spherical joint between the frame and the mobile platform. Of course this 3-CRU+S solution further increases the degrees of constraint of the structure and limits the accessibility of motion centre for the possible practical applications of the wrist.

6.1 Design of the limbs

As a matter of fact, the whole flexures-based mini-wrist (i.e. the three CRU limbs and the mobile platform) is just one solid piece of material, properly connected to the ground and to the linear actuators; anyway, as a first approximation, the entire compliance of the structure can be lumped by considering one flexible leg of the manipulator as a series of rigid links connected by elastic hinges (pseudo-rigid-body model). An ordinary flexure hinge provides a relationship between the applied moment **M** and the resulting rotation **Φ** given by **Φ** = **ZM**, where **Z** is the full *3x3* compliance matrix: a proper design of the flexure hinge requires a dominant diagonal matrix **Z**, in order to reduce the coupling effects. Furthermore the ratio between yield strength (σ_{yi}) and elastic Young modulus (E) of the material heavily affects the limits of rotation of flexure hinges therefore in order to obtain a larger workspace, a material with a high ratio σ_{yi}/E must be selected (the *Ti-10V-2Fe-3Al* alloy in this preliminary design, having $E = 103\ GPa$, Poisson's modulus of *0.34* and $\sigma_{yi} = 1200\ MPa$).

Figure 12 shows the design adopted for each limb of the manipulator: the legs are tilted with respect to the vertical plane thus allowing the platform to avoid singular poses [21]. The relationships between $\hat{\mathbf{w}}_{ji}$ (j = 1,2,3,4; i = 1,2,3) discussed in previous section 3.2 are granted as well.

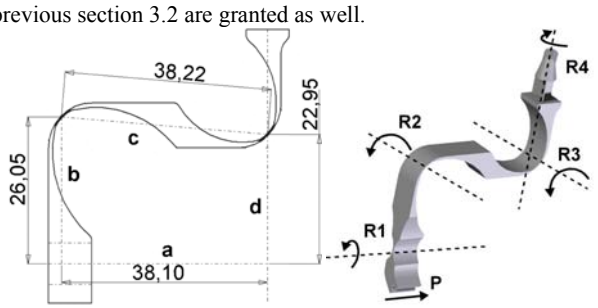

Fig. 12. Design of the legs

The cylindrical joint (C) is substituted by a linear pair (P) in series with a double notch flexure hinge (R1) with constant radius $r = 5\ mm$, smallest thickness $t = 0.4\ mm$ and width $w = 8\ mm$. The compliance of the flexure hinge around its compliance axis may be estimated by the following formula:

$$\delta_{b1} = \frac{9\pi r^{0.5}}{2Ewt^{2.5}} = 0.37 \cdot 10^{-3}\, rad / Nmm \tag{46}$$

which clearly shows that the compliance mostly depends on the thickness t. The intermediate revolute pair (R2) and the first revolute pair of the universal joint (R3) were designed as single notch flexure hinges but with radius taken constant only for 11% of the entire angle span (π/6 against 3π/2): the geometrical data of the hinges are $r = 7.7\ mm$, $w = 8\ mm$, $t = 0.3\ mm$. In these cases the theoretical formula for the single notch hinge with constant radius, different from (46) only for the values of the coefficients, may not provide a correct evaluation of the compliance and therefore it was used only for a preliminary design: a finite element model of R2 and of R3 has been developed instead. The FEM model of the flexure hinge was loaded by a given bending moment around the compliance axis and rigidly constrained at one end, then the arising rotation has been calculated: the resulting stiffness values are respectively $\delta_{b2} = 2.6 \cdot 10^{-3}\, rad / Nmm$ and $\delta_{b3} = 2.1 \cdot 10^{-3}\, rad / Nmm$. Figure 13 shows details of the R1, R2, R3 and R4 pairs of the leg: all the revolute pairs must be stiff with respect to moments applied around the other two axes in order to reduce the influences of the warping phenomena of the entire leg.

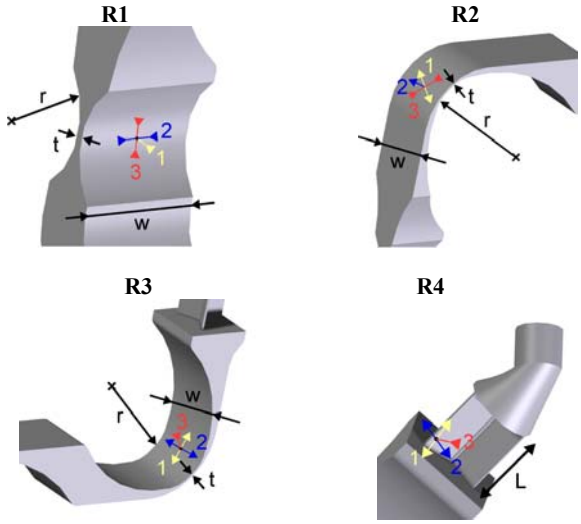

Fig. 13. Details of the flexure hinges R1, R2, R3 and R4 (the directions of the principal stresses at one sample point are shown with indication of the traction/compression state)

The second pair of the universal joint (R4) has been a crucial step of leg's design because of the strict geometrical requirements imposed by the $\mathbf{w}_{ji}$ alignment. The pair must work as a torsion bar along its local axis but, at the same time, it must be able to resist to the bending actions along the other two axes. For that reason a cross section was recknoned as the most appropriate, with three symmetric plates having thickness $t_i = 0.25\ mm$ and width $w_i = 2.78\ mm$. The torsion compliance δ_{t4} of the column is given by:

$$\delta_{t4} = \frac{L}{GJ_p} \tag{47}$$

where G is the shear modulus of the material, L is the height of the column and J_p is the second moment of area around the torsion axis. In case of cross sections it holds $J_p \cong \frac{1}{3}\sum_i^N w_i t_i^3$: it is worth noting that the compliance mostly depends on t_i. The strength of the column to bending moments does not allow to increase the height L as desirable. The numerical calculation of the compliance of the torsion bar provides $\delta_{t4} = 2.2 \cdot 10^{-3}\, rad / Nmm$ which is close to the approximated value provided by (47).

6.2 Elasto-static analysis

The entire 3-CRU+S manipulator has been modeled by finite elements, using a quadratic tetrahedral element for the parameterization; the final mesh consisted of 27 471 nodes and 14 857 elements. The model has been loaded by imposing the displacements a_i (i=1,2,3) of the actuated frame sliders: in order to evaluate the workspace of the moving platform and to be sure to assess the mechanical resistance of the structure in all the poses of interest, 5^3 loading cases have been considered, by assigning to each axis five strokes of the same length, starting from the home position to end up at the maximum allowed travel of the slider, i.e. $-5\ mm \le a_i \le 5\ mm$. At each pose a stress-displacement analysis has been executed by means of the FEM model: at each step the results have been obtained at the end of an iterative calculation

using the Newton-Raphson method because of the geometrical non-linearity of the problem.

The analysis of the 5^3 loading cases showed that only in few of them (16 configurations) the computed stresses were slightly over the limit of the yielding strength of the material. The displacements of the moving platform and the stresses in the structure are shown in Fig. 14a and 14b when the legs 1 and 3 are moved 5 *mm* upwards and the leg 2 is moved 5 *mm* downwards: this is one of the most critical poses of the manipulator from a structural point of view. It can be noted the symmetry of the displacement field of the moving platform: points *A* and *B*, which are two vertexes, undergo maximum displacements of about *16 mm*; it is recalled that the centre of the spherical motion *C* is constrained to the frame.

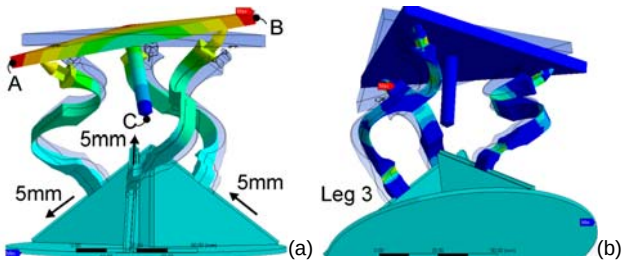

Fig. 14. FEM model of the 3-CRU+S wrist: field of displacements (a) and Von Mises equivalent stresses (b)

The equivalent Von Mises stresses are mapped in Fig. 14b while Tab. 4 collects the maximum measured value for each flexure; it further shows the three principal stresses at one point that is located at the geometric centre of the joint, lying on one of the two lateral surfaces (the corresponding principal directions and the measured points are shown in Fig. 13 for each joint).

Table 4. Principal stresses of leg's flexures and Von Mises equivalent values

Hinge	R1	R2	R3	R4
Von Mises equivalent stress [MPa]	1124	583	743	1180
Principal stresses [MPa]	σ_1 = -13 σ_2 = -280 σ_3 = -779	σ_1 = 58 σ_2 = 14 σ_3 = -132	σ_1 = 791 σ_2 = 234 σ_3 = -52	σ_1 = 1166 σ_2 = 97 σ_3 = -37

Some considerations on the structural behavior of the manipulator may be drawn from the results of FEM simulations. In all flexures, the reduced thickness of the bending arcs yields plane stresses in the corresponding sections. In the measurement point of R1, the smallest stress is directed along the normal to flexure profile while the maximum value, σ_3, represents a compression on one face and a tensile stress on the other one, thus evidencing the bending of the profile caused by the motion of the frame slider: the high ratio σ_3/σ_1 shows that the design is good and the flexure works properly, even if the stretching actions are developed at the extremes of the leg and therefore pretty far from flexure ends. The equivalent stresses of Tab. 4 show that flexures 2 and 3 are less loaded than R1 and R4, that is also in accordance with the limited stroke of R2, see Tab. 5; the same considerations drawn for R1 can be repeated for R2 and R3; the opposite sign of σ_1, σ_3 in the R2 flexure shows that the leg presents in the R2 hinge a local warping displacement. The higher value of σ_1 in R3 flexure and its actual direction (that is tangent to the profile) testify a better behavior with respect to the R2 case. Flexure R4 is characterized by the most complicated design thus its state of stress is complex as well and heavily loaded: the stresses due to the correct torsion behavior of the hinge are mixed with the stresses arising for the stretching and the bending of the column; the latter effects are basically due to the geometrical requirements imposed to the column bending because of the large slope of its axis with respect to the plane of the moving platform.

The model allowed also to compute the range of (equivalent) rotations of the flexures when the wrist is moved throughout the restricted orientation workspace defined by the inner sphere shown in Fig. 15: the results are shown in Tab. 5: it may be interesting to compare such results with the correspondent rotations provided by the rigid body model in Tab. 2.

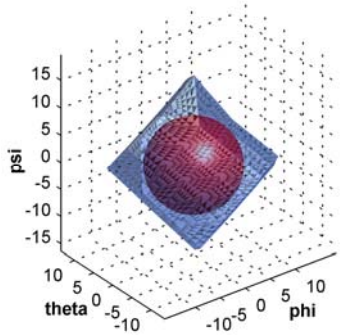

Fig. 15. The Tait-Bryan angles workspace of the 3-CRU+S wrist (by FEM analysis of flexible model)

It may be noticed that R1, R3 and R4 have symmetric working ranges and that R2 has a very small range of rotation. Such limited rotations yield a very small working space, that is represented by means of the usual Tait-Bryan angles set (φ,θ,ψ) in Fig. 15: the largest sphere completely inscribed in it has a radius of about *8°*.

The finite element analysis also provides the forces required by the linear motors to drive the platform inside the (restricted) workspace in the static case: a maximum actuation force of *21 N* is required in the worst case; moreover, the maximum value of the constraint force at the ball joint *C* was calculated to be 60 *N*, therefore allowing the possible use of a magnetic spherical bearing. These data can be useful for choosing appropriate linear motors and joints.

7 Conclusions

The article has described all the main design steps of a mini robotic wrist whose kinematics is based in the end on the 3-CRU+S structure: such architecture is suitable to be realized by means of flexible joints and powered by commercial mini-actuators. Such wrist could be used in miniaturized assembly stations for the orientation of mini or micro-objects and interfaced with other mini-devices; the orientation of lasers, cameras or high accuracy instruments in the space are also possible applications.

A differential kinematic analysis has shown that the singularity surfaces limit its workspace to a region that, for the rigid body model of the wrist, can be represented in the orientation space by a sphere with a radius of 31°. Then inverse dynamics simulations showed that for motions with frequency below *1 Hz* the contributions of dynamic terms is negligible or comparable with static forces, while high speeds motions would require a model of the vibration behavior of the machine itself.

Another constraint for the operative workspace is represented by the actual strokes of the passive joints which, being realized with the technique of the flexible joints, have a maximum deformability that depends on the chosen material and on path planning. Therefore in this case joints' design had to be integrated into the dimensioning of the legs of the manipulator and finally of the whole platform.

Then the geometry of the joints themselves has been defined according to the needed mobility, the geometry of the single leg and the limitations on their dimensions; then the strain and the stress of joints and legs in each feasible configuration of the workspace have been analyzed and compared with the available performances of the material.

Finite element simulations allowed also to establish the estimated workspace of the machine by taking into account the actual behavior of the flexures and the properties of the selected material: it resulted that the use of flexures reduces the effective workspace as much as a resulting a shallow volume enveloping a sphere of 8° radius; this value is very small indeed, therefore a real implementation of the design could not do without reconsidering the design choices, that should be aimed at an enlargement of the workspace. It must also be noted that, due to the highly over-constrained nature of the flexible link manipulator, the (theoretical) centre of spherical motion moves around in the workspace with pretty large displacements. Therefore it has been proposed to use a ball joint to constrain the platform to the ground: such modification of the original concept seems feasible from the structural point of view but prevents the accessibility of motion centre for the possible applications. An alternative opportunity would be the redesign of platform's legs aiming at minimizing this unwanted side-effect, instead of searching for maximum flexures displacements.

Table 5. Motion range of the passive joints (flexible links model)

	$\boldsymbol{\theta}_{1i}$			$\boldsymbol{\theta}_{2i}$			$\boldsymbol{\theta}_{3i}$			$\boldsymbol{\theta}_{4i}$		
	$\boldsymbol{\theta}_{1i}^{(\min)}$	$\boldsymbol{\theta}_{1i}^{(\max)}$	$\Delta\boldsymbol{\theta}_{1i}$	$\boldsymbol{\theta}_{2i}^{(\min)}$	$\boldsymbol{\theta}_{2i}^{(\max)}$	$\Delta\boldsymbol{\theta}_{2i}$	$\boldsymbol{\theta}_{3i}^{(\min)}$	$\boldsymbol{\theta}_{3i}^{(\max)}$	$\Delta\boldsymbol{\theta}_{3i}$	$\boldsymbol{\theta}_{4i}^{(\min)}$	$\boldsymbol{\theta}_{4i}^{(\max)}$	$\Delta\boldsymbol{\theta}_{4i}$
$i = 1$	-8.1°	+7.9°	16.0°	-0.3°	0°	0.3°	-7.6°	+8.3°	15.9°	-7.9°	+8.1°	16.0°
$i = 2$	-7.9°	+8.1°	16.0°	-0.3°	0°	0.3°	-7.7°	+8.2°	15.9°	-8.0°	+8.0°	16.0°
$i = 3$	-8.0°	+8.0°	16.0°	-0.3°	0°	0.3°	-7.5°	+8.4°	15.9°	-8.1°	+7.9°	16.0°

8 References

[1] Clavel, R., 1988, "Delta, a fast robot with parallel geometry", *Proc. 18th ISIR: Intl. Symp. on Industrial Robots*, Lausanne, Apr. 26-28, pp 91-100.

[2] Tsai, L.W. and Joshi, S., 2002, "Kinematics Analysis of 3-DOF Position Mechanisms for Use in Hybrid Kinematic Machines", ASME J. Mech. Design, **124**, pp.245-253.

[3] Callegari, M. and Tarantini, M., 2003, "Kinematic Analysis of a Novel Translational Platform", ASME J. Mech. Design, **125**(2), pp.308-315.

[4] Liu, X., Wang, J. and Pritschow, 2005, "A New Family of Spatial 3-DoF Fully-Parallel Manipulators with High Rotational Capability", Mechanism and Machine Theory, **40**, pp.475-494.

[5] Li, W., Gao, F. and Zhang, J., 2005, "R-CUBE, a Decoupled Parallel Manipulator only with Revolute Joints", Mech. Mach. Theory, **40**, pp. 467-473.

[6] Callegari, M. and Palpacelli, M.-C., 2008, "Prototype design of a translating parallel robot", Meccanica, **43**(2), pp.133-151.

[7] Callegari, M., Gabrielli, A. and Ruggiu, M., 2008, "Kineto-Elasto-Static Synthesis of a 3-CRU Spherical Wrist for Miniaturized Assembly Tasks", Meccanica, **43**(4), pp.377-389.

[8] Gosselin, C. and Angeles, J., 1989, "The optimum kinematic design of a spherical three-degree-of-freedom parallel manipulator", ASME J. Mechanisms, Transmissions and Automation in Design, **111**(2). pp.202-207.

[9] Lee, J.J. and Chang, S.-L., 1992, "On the kinematics of the UPS wrist for real time control", *Proc. 22nd ASME Biennal Mechanisms Conference: Robotics, Spatial Mechanisms and Mechanical Systems*, Scottsdale, USA, Sept. 13-16, pp.305-312.

[10] Innocenti, C. and Parenti-Castelli, V., 1993, "Echelon form solution of direct kinematics for the general fully-parallel spherical wrist", Mech. Mach. Theory, **28**(4), pp.553-561.

[11] Alizade, R.I., Tagiyev, N.R. and Duffy, J., 1994, "A forward and reverse displacement analysis of an in-parallel spherical manipulator", Mech. Mach. Theory, **29**(1), pp.125-137.

[12] Kong, X. and Gosselin, C.M., 2004, "Type synthesis of 3-DOF spherical parallel manipulators based on screw theory", ASME J. Mech. Design, **126**(1), pp.101-108.

[13] Kong, X. and Gosselin, C.M., 2004, "Type synthesis of three-degree-of-freedom spherical parallel manipulators", Intl J. of Robotics Research, **23**(3), pp.237-245.

[14] Karouia, M. and Hervé, J.M., 2006, "Non-overconstrained 3-dof spherical parallel manipulators of type: 3-RCC, 3-CCR, 3-CRC", Robotica, **24**(1), pp.85-94.

[15] Karouia, M. and Hervè, J.M., 2002, "A Family of Novel Orientational 3-DOF Parallel Robots", *Proc. 14th RoManSy*, Udine, Italy, July 1-4, pp. 359-368.

[16] Fang, Y. and Tsai, L.-W., 2004, "Structure synthesis of a class of 3-DOF rotational parallel manipulators", IEEE Trans. on Robotics and Automation, **20**(1), pp.117-121.

[17] Di Gregorio, R., 2001, "Kinematics of a new spherical parallel manipulator with three equal legs: the 3-URC wrist", J. Robotic Systems, **18**(5), pp.213-219.

[18] Di Gregorio, R., 2001, "A new parallel wrist using only revolute pairs: the 3-RUU wrist", Robotica, **19**(3), pp.305-309.

[19] Di Gregorio, R., 2004, "The 3-RRS Wrist: A New, Simple and Non-Overconstrained Spherical Parallel Manipulator", ASME J. Mech. Design, **126**(5), pp.850-855.

[20] Lusk, C.P. and Howell, L.L., 2008, "Spherical Bistable Micromechanism", ASME J. Mech. Design, **130**(4), pp.045001-1:6.

[21] Callegari, M., 2008, "Design and Prototyping of a SPM Based on 3-CPU Kinematics", In: *Parallel Manipulators: New Developments*, Jee-Hwan Ryu ed., I-Tech publ. Vienna. pp. 171-198. (open access at http://books.i-techonline.com/)

[22] Pernette, E., Henein, S., Magnani, I. and Clavel, R., 1997, "Design of parallel robots in microrobotics", Robotica, **15**, pp.417-420.

[23] Yi, B.-J., Chung, G.B., Na, H.Y., Kim, W.K. and Suh, I.H., 2003, "Design and experiment of a 3-DOF parallel micromechanism utilizing flexure hinges", IEEE Trans. Robotics and Automation, **19**(4), pp.604-612.

[24] Lusk, C.P. and Howell, L.L., 2008, "Components, Building Blocks, and Demonstrations of Spherical Mechanisms in Microelectromechanical Systems", ASME J. Mech. Design,, **130**(3), pp.034503-1:4.

[25] Bertetto A.M. and Ruggiu M., 2003, "A Two Degree of Freedom Gripper Actuated by SMA with Flexure Hinges", J Robotic System, **20**, pp. 649-657

[26] Kang, B.H., Wen, J.T., Dagalakis, N.G. and Gorman, J., 2004, "Analysis and Design of Parallel Mechanism with Flexure Joints", *Proc. IEEE Int. Conf. on Robotics and Automation*, New Orleans, Apr. 28-30, pp.4097-4102.

[27] Li Y., Xu Q., 2005, "Design and Analysis of a New 3-DOF Compliant Parallel Positioning Platform for Nanomanipulation", *Proc. 5th IEEE Conference on Nanotechnology*, Nagoya, Japan, July 11-15.

[28] Li Y., Xu Q., 2005, "Kinematic Design of a Novel 3-DOF Compliant Parallel Manipulator for Nanomanipulation", *Proc. IEEE/ASME Int. Conf. on Advanced Intelligent Mechatronics*, Monterey, USA, pp.93-98.

[29] Xu, Q. and Li, Y., 2006, "Kinematic Analysis and Optimization of a New Compliant Parallel Micromanipulator", Intl. J. Advanced Robotic Systems, **3**(4), pp.351-358.

[30] Paros, J.M. and Weisbord, L., 1965, "How to Design Flexure Hinges", Machine Design, **37**, pp.151-156.

[31] Moon, Y.M., Trease, B.P. and Kota, S., 2005, "Design of Large-Displacement Compliant Joints", ASME J. Mech. Design, **127**, pp.788-798.

[32] Callegari, M., Cammarata, A., Gabrielli, A., and Sinatra, R., 2007, "Kinematics and Dynamics of a 3-CRU Spherical Parallel Robot", *Proc. 31st ASME Mechanisms and Robotics Conference (MECH)* held within the *Intl. Design Engineering Technical Conferences & Computers and Information in Engineering Conference, IDETC/CIE 2007*, Las Vegas, USA, Sept. 4-7, 2007. Paper n° DETC2007-35894.

[33] Angeles, J. and Khan, W.A., 2006, "The kinetostatic optimization of robotic manipulators: the inverse and the direct problems", ASME J. Mech. Design, **128**(1), pp. 168–178.

[34] Angeles, J., 2007, *Fundamentals of Robotic Mechanical Systems*, 3rd ed., Springer, New York.

[35] Angeles, J. and Lee, S., 1988, "The Formulation of Dynamical Equations of Holonomic Mechanical Systems Using a Natural Orthogonal Complement", ASME J. Applied Mechanics, **55**, pp. 243-244.

[36] Yoshikawa, T., 1985, "Dynamic Manipulability of Robot Manipulators", J. Robotic Systems, **2**, pp.113-124.

[37] Yoshikawa, T., 2000, "Erratum to 'Dynamic Manipulability of Robot Manipulators'", J. Robotic Systems, **17**(8), pp. 449.